

Triarylphosphine-Stabilized Platinum Nanoparticles in Three-Dimensional Nanostructured Films as Active Electrocatalysts

Cynthia N. Kostelansky, Jeremy J. Pietron, Mu-San Chen, Walter J. Dressick, Karen E. Swider-Lyons, David E. Ramaker, Rhonda M. Stroud, Christopher A. Klug, Brian S. Zelakiewicz, and Terence L. Schull*

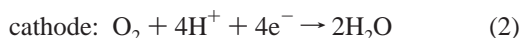
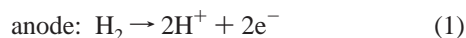
Naval Research Laboratory, 4555 Overlook Avenue, SW, Washington, District of Columbia 20375

Received: May 1, 2006; In Final Form: August 7, 2006

Ligand-stabilized platinum nanoparticles (Pt NPs) can be used to build well-defined three-dimensional (3-D) nanostructured electrodes for better control of the catalyst architecture in proton exchange membrane fuel cells (PEMFCs). Platinum NPs of 1.7 ± 0.5 nm diameter stabilized by the water-soluble phosphine ligand, tris(4-phosphonatophenyl)phosphine (TPPTP, $P(4-C_6H_4PO_3H_2)_3$), were prepared by ethylene glycol reduction of chloroplatinic acid and subsequent treatment of the isolated nanoparticles with TPPTP. The isolated TPPTP-stabilized Pt NPs were characterized by multinuclear magnetic resonance spectroscopy (^{31}P and ^{195}Pt NMR), high-resolution transmission electron microscopy (HRTEM), X-ray photoelectron spectroscopy (XPS), and extended X-ray absorption fine structure (EXAFS). The negatively charged TPPTP–Pt NPs were electrostatically deposited onto a glassy carbon electrode (GCE) modified with protonated 4-aminophenyl functional groups (APh). Multilayers were assembled via electrostatic layer-by-layer deposition with cationic poly(allylamine HCl) (PAH). These multilayer films are active for the key hydrogen fuel cell reactions, hydrogen oxidation (anode) and oxygen reduction (cathode). Using a rotating disk electrode configuration, fully mass-transport limited kinetics for hydrogen oxidation was obtained after 3 layers of TPPTP–Pt NPs with a total Pt loading of $4.2 \mu g/cm^2$. Complete reduction of oxygen by four electrons was achieved with 4 layers of TPPTP–Pt NPs and a total Pt loading of $5.6 \mu g/cm^2$. A maximum current density for oxygen reduction was reached with these films after 5 layers resulting in a mass-specific activity, i_m , of $0.11 A/mg_{Pt}$ at 0.9 V. These films feature a high electrocatalytic activity and can be used to create systematic changes in the catalyst chemistry and architecture to provide insight for building better electrocatalysts.

1. Introduction

Proton exchange membrane fuel cell (PEMFC) electrodes are heterogeneous supported catalyst structures with electrocatalytic activities that are greatly affected by the microenvironment surrounding the catalyst particles. The most widely used electrocatalysts to date for both the hydrogen oxidation reaction (HOR) at the anode (eq 1) and the oxygen reduction reaction (ORR) at the cathode (eq 2) are platinum nanoparticles dispersed on porous, electronically conductive Vulcan carbon supports.¹



The electrochemical performance of these catalysts needs improvement, especially at the cathode, where the ORR suffers from slow kinetics. The kinetic limitations result in high overpotentials² and require the use of platinum loadings too high for viable commercial use.³ Strategies for improving the electrocatalytic activity of these Pt-based catalysts mainly consist of combining Pt with other transition metals,⁴ replacing Pt altogether with other less expensive metals,⁵ or tailoring the Pt particle size to control the relative fraction of Pt surface atoms.⁶

It is well-known in homogeneous catalysis that the reactivity and selectivity of metal-catalyzed reactions can be influenced

by the ligands used to stabilize the metal center. Schmid and co-workers have demonstrated that these same principles can be applied to supported ligand-protected nanoparticles.⁷ They showed that the hydrogenation of 2-hexyne with a phenanthroline-stabilized Pd nanocluster supported on active carbon gives a mixture of *trans/cis*-2-hexene. Simply changing the supporting ligand to 3-*n*-butyl-phenanthroline altered the reaction significantly giving only one isomer, *cis*-2-hexene, in significantly less time. We envision applying these principles of homogeneous catalysis to the design of PEMFC electrodes. Our approach is to place well-defined ligand-stabilized Pt NPs uniformly on the electrode surface to better control the catalyst architecture and increase accessibility to the active catalytic sites.

Ligands not only can affect the selectivity of metal nanoparticles, but they can also influence the electronic properties of the metal core.⁸ Even small changes in the protecting ligand shell can lead to varying electronic properties of the metal core as was seen with $N(\text{alkyl})_4\text{Cl}$ -stabilized Pd nanoparticles.^{8a,b} This ligand sensitivity allows for tuning of the platinum nanoparticles' electronic state by simply changing the protecting ligand shell. Recently, ligand-stabilized platinum nanoparticles have received attention as electrocatalysts.⁹ The ligands not only can influence the electronic properties of the platinum nanoparticle, but they can also serve to enable the engineering of three-dimensional (3-D) nanostructured catalysts through electrostatic layer-by-layer (LBL) deposition.

The LBL deposition of polyelectrolyte multilayers is an inexpensive and easy way to prepare uniform thin films with a

* To whom correspondence should be addressed. Phone: (202) 404-6043; fax: (202) 767-9594; e-mail: schull@nrl.navy.mil.

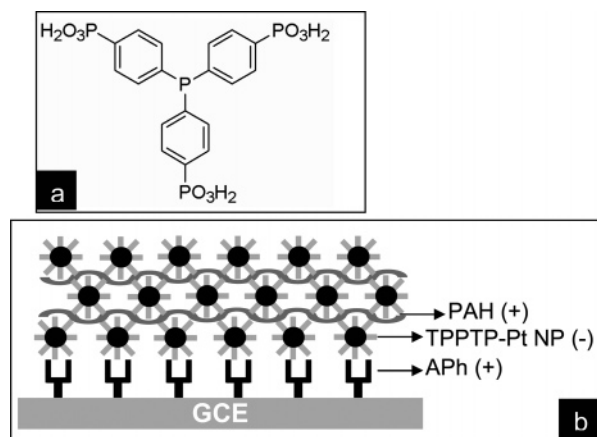


Figure 1. (a) Structure of anionic tris(4-phosphonatophenyl)phosphine, TPPTP and (b) depiction of 3 layers of TPPTP–Pt NPs using PAH spacer layers on a glassy carbon electrode surface modified with APh functional groups.

wide variety of chemical and physical properties.¹⁰ Halaoui et al. recently reported that polyacrylate-capped Pt NPs deposited in a polyelectrolyte matrix were electrochemically active for both HOR and ORR.^{10b} Similarly, citrate-stabilized Pt NPs alternately assembled with metalloporphyrins catalyze an almost four-electron reduction of oxygen.^{10e} Importantly, these results indicate that mass transport and charge transfer required for fuel cell electrocatalysts are feasible in these films, and as a result, they are promising candidates for new nanostructured architectures for PEMFCs. Presently, it is difficult to compare the activity of these electrodes to state-of-the-art platinum catalysts because HOR and ORR were not measured using the more standard methodology of thin-film rotating disk electrode (RDE) characterization in perchloric acid.^{11,12} We apply this RDE methodology to compare our new catalyst architectures to state-of-the-art PEMFC catalysts. This allows for the extraction of meaningful kinetic HOR and ORR data directly using the unmodified mass-transport correlations for a smooth RDE, which in turn can be used to predict fuel cell performance.

We report the synthesis and characterization of Pt NPs stabilized by the water-soluble phosphine ligand, P(4-C₆H₄-PO₃H₂)₃ (tris(4-phosphonatophenyl)-phosphine, TPPTP),¹³ and their use in nanostructured thin films as electrocatalysts for the key hydrogen fuel cell reactions. The anionic phosphonate groups of the ligand (Figure 1a) impart water solubility to the nanoparticles, allowing them to be easily incorporated into polyelectrolyte multilayers in aqueous media. Multilayers of TPPTP–Pt NPs assembled via electrostatic LBL deposition with cationic poly(allylamine HCl) (PAH) on a protonated 4-aminophenyl (APh)-modified GCE (Figure 1b) are highly active electrocatalysts for both HOR and ORR. This approach is our first step toward building controlled 3-D architectures that can be used for systematic studies involving changing the ligand, support, nanoparticle size, and spacing to aid in the design of more active electrocatalysts for PEMFCs.

2. Experimental Procedures

2.1 Materials. Hydrogen hexachloroplatinate(IV) hexahydrate (H₂PtCl₆·6H₂O, Strem), Sephadex LH-20 (Amersham Bioscience), tetrabutylammonium tetrafluoroborate (TBA⁺BF₄[−], Aldrich), tetrabutylammonium bromide (TBA⁺Br[−], Aldrich), acetonitrile (ACN, Aldrich, Sure/Seal), and poly(allylamine hydrochloride) (PAH, average molecular weight 15 000 g/mol, Aldrich) were used as received. Tris(4-phosphonatophenyl)-

phosphine (TPPTP)¹³ and (4-nitrophenyl)diazonium tetrafluoroborate¹⁴ were synthesized according to published procedures. *N*-(2-Aminoethyl)-3-aminopropyltrimethoxysilane (EDA, Gelest, Inc.) was purified by vacuum distillation (140 °C, 14 mmHg) and stored under a dry nitrogen atmosphere until needed for use. Optical grade polished fused silica (FS) slides (25 mm × 25 mm × 1 mm) were purchased from Dell Optics Inc. All aqueous solutions were prepared with water purified by a Millipore Milli-Q Plus system to 18.2 MΩ cm.

2.2 Synthesis of Pt Nanoparticles. Glycol-Stabilized Pt NPs. Pt nanoparticles stabilized by glycol and OH[−] were prepared according to a previously reported method.¹⁵ Briefly, a solution of H₂PtCl₆·6H₂O (791 mg, 1.93 mmol) in ethylene glycol (50 mL) was added to a 0.5 M solution of NaOH in ethylene glycol (50 mL). The resulting orange–yellow solution was heated to 160 °C for 3 h under reflux. A transparent brown Pt colloidal solution was obtained and stored under N₂.

TPPTP-Stabilized Pt NPs. The glycol-stabilized Pt NPs (30 mL, 0.579 mmol of Pt) were isolated as a brown solid via precipitation with 0.1 M HCl until a pH value of less than 4 was reached. After centrifugation, the isolated Pt NPs were dispersed in a minimal amount of acetone and precipitated with 0.1 M HCl, followed by centrifugation to isolate the brown Pt NPs. This was repeated 3 times to remove excess ethylene glycol. The isolated Pt NPs were dispersed in degassed acetone (5 mL) and added to a solution of TPPTP (0.153 g, 0.290 mmol) in degassed water (15 mL), resulting in a homogeneous brown dispersion. This dispersion was mechanically stirred under N₂ for 1 h to allow for partial exchange of the TPPTP ligand at the platinum surface. The solvent mixture was then removed in vacuo, and degassed water (15 mL) was added resulting in a transparent brown Pt colloidal dispersion. After 24 h of stirring under N₂, a solution of 30 wt % NaOH (0.5 mL) was added to precipitate a brown solid that was collected by centrifugation, redispersed in water (15 mL), and allowed to stir under N₂ to complete the ligand exchange. Complete exchange of the TPPTP ligand at the Pt NP surface required several days. The ligand exchange was monitored by solution ³¹P NMR spectroscopy. Once no free TPPTP ligand was observed by ³¹P NMR, the solvent was removed in vacuo. To remove the excess free TPPTP oxide formed during the ligand exchange process, the crude material was redispersed in a minimal amount of water and purified by gel-filtration chromatography using Sephadex LH-20.¹⁶ The brown–yellow layer was collected, and the water was removed in vacuo to give a black solid that was completely redispersible in water. Multiple elemental analyses by ICP (Robertson Microlit Laboratories) showed a Pt metal content in the range of 66.08–58.25% and a P content of 5.91–4.47% corresponding to a Pt/TPPTP ratio of ~7:1.

2.3 Characterization of TPPTP–Pt NPs. Nuclear Magnetic Resonance Spectroscopy. Solution ¹H and ³¹P NMR spectra were recorded on a Bruker DRX 400 spectrometer and referenced to residual ¹H signals of the deuterated water (¹H) or external H₃PO₄ (³¹P). All ¹⁹⁵Pt solid-state nuclear magnetic resonance (ss-NMR) studies were performed at room temperature (298 K) at 11.7 T on a Bruker Digital DMX500 spectrometer interfaced with a Silicon Graphics console running the XWINNMR 2.6 software package. Approximately 100 mg of the isolated TPPTP–Pt NPs solid was loosely packed into a 4 mm sample vial under ambient conditions. Data were acquired on a point-by-point basis under static conditions using a simple Hartman–Hahn solid-state echo pulse sequence with a recycle delay of 25 ms and a τ of 20 μ s.

X-ray Photoelectron Spectroscopy. XPS spectra were acquired using a Thermo VG Scientific Escalab 220i-XL with a monochromatic Al K α source. Carbon paper modified with negatively charged TPPTP–Pt NPs, as described in Electrochemical Measurements, was dried overnight before placing it in the UHV chamber. Measurements were performed at room temperature with a base pressure of 1×10^{-9} Torr. Survey scans were performed from 0 to 1400 eV binding energies and 100 eV pass energy. High-resolution scans of Pt 4f and 4d, O 1s, C 1s, N 1s, and P 2p were acquired with 15–20 eV windows and a 20 eV pass energy. The core-level binding energies were calibrated to the C 1s peak at 284.4 eV. The high-resolution spectra were fit using Unifit software.¹⁷

Transmission Electron Microscopy. High-resolution TEM was performed on a JEOL JEM-2200FS microscope operating at a 200 kV accelerating voltage. Samples were prepared by placing a drop of an aqueous TPPTP–Pt NP dispersion (0.25 mg/mL in the presence of a surfactant, ca. 10 mg of tetrabutylammonium bromide) on a 300 mesh copper grid coated with continuous carbon film (Ted Pella). The samples were dried overnight in vacuo. Images were recorded using a Gatan Ultrascan CCD camera, and the camera constants were calibrated using gold lattice images. Pt core diameters were measured using the Image Processing Tool Kit plug in for Photoshop. A total of 214 particles were measured, resulting in an average core diameter of 1.7 ± 0.5 nm. The electron diffraction pattern exhibited four diffraction rings that corresponded to the d spacings for the (111), (200), (220), and (311) planes of a face centered–cubic platinum structure.

Extended X-ray Absorption Fine Structure. EXAFS measurements of TPPTP–Pt NPs were taken in fluorescent mode at beamline X11B at the National Synchrotron Light Source (NSLS) at Brookhaven National Laboratory. The spectra were collected on a monolayer of TPPTP–Pt NPs deposited on grafted carbon paper as described in Electrochemical Measurements. Data analysis was performed with the IFEFFIT program¹⁸ using an R -range of 0.5–2.8 Å and the Fourier transform k^3 ($2 < k < 11$) for the PtPt and PtO scattering paths. The data from $k > 11$ were not useful due to background noise in the spectra from these low-platinum films. The atomic EXAFS contribution below $R = 3$ Å was reduced by adjusting the R_{bkg} parameter in the Athena code of the IFEFFIT package.¹⁸

UV–Visible Spectroscopy. UV–vis spectra, corrected for baseline variations using EDA-coated fused silica reference slides, were acquired using a Varian Cary 5000 double-beam spectrophotometer as described elsewhere.¹⁹ EDA self-assembled monolayers were chemisorbed onto freshly cleaned fused silica slides using the literature procedure.²⁰ TPPTP–Pt NPs/PAH multilayers were then fabricated on the EDA-coated fused silica slides via dip coating from a stirred aqueous TPPTP–Pt NPs dispersion (0.3 mg/mL) and PAH (2 mg/mL) solution, each containing 0.01 M HCl and 0.01 M NaCl for control of the pH and ionic strength. A programmed StratoSequence VI robot dip coater (nanoStrata Inc.) was used to deposit each layer of the film, with deposition times of 120 min for the TPPTP–Pt NPs dispersion and 30 min for the PAH solution. The treated fused silica slides were automatically triple rinsed using deionized water (1 min per rinse cycle) and dried in a filtered N₂ gas stream (30 s) following deposition of each layer.

2.4 Electrochemical Measurements. Grafting of Carbon Electrode. The surface of the glassy carbon electrode (GCE) was grafted with a monolayer of 4-aminophenyl (Aph) functional groups according to a published procedure.²¹ Briefly, glassy carbon disk electrodes (5.0 mm diameter, 0.196 cm², Pine

Instruments) polished to a mirror finish with 0.1 μm alumina powder on a polishing cloth (Buehler) were suspended under Ar in a solution of freshly prepared 5 mM (4-nitrophenyl)-diazonium tetrafluoroborate and 0.1 M TBA⁺BF₄[–] in acetonitrile. Electrolysis at -1.1 V versus Ag/Ag⁺ for 10 min resulted in the covalent attachment of 4-nitrophenyl functional groups to the electrode surface, as confirmed by the reversible wave observed in the cyclic voltammetry in pure electrolyte. Reduction of the nitro group to an amine was achieved by applying a potential of -1.2 V for 10 min in a protic solution (0.1 M KCl in 90:10 water/ethanol), resulting in the formation of Aph functional groups on the GCE surface. The Aph-modified GCE (GCE-Aph) was immersed into a 0.1 M HClO₄ solution for 10 min to protonate the amine group, resulting in a uniform positively charged surface to which the negatively charged TPPTP–Pt NPs can electrostatically bind.

Electrode Assembly. Multilayer assemblies of TPPTP–Pt NPs were assembled via electrostatic layer-by-layer deposition with poly(allylamine hydrochloride) (PAH) on the protonated Aph-modified GCE. To assemble TPPTP–Pt NPs/PAH multilayers, the protonated GCE-Aph electrode was dipped into a 0.01 M HCl/0.01 M NaCl_(aq) solution containing the TPPTP–Pt NPs (15 mg/50 mL) for 24 h and rinsed with water, resulting in a 1 layer TPPTP–Pt NP electrode designated as GCE-Aph/TPPTP–Pt NP. Additional TPPTP–Pt NP layers were added as required by sequential immersion in 0.01 M HCl/0.01 M NaCl_(aq) solution containing PAH (2 mg/mL) for 30 min, rinsing in water, immersion in 0.01 M HCl/0.01 M NaCl_(aq) solution containing the TPPTP–Pt NPs (15 mg/50 mL) for 24 h, and rinsing again in water. The composition of the electrode so obtained is indicated by the shorthand notation, GCE-Aph/TPPTP–Pt NP/(PAH/TPPTP–Pt NP) _{$n-1$} , where n is the total number of TPPTP–Pt NP layers present following $n - 1$ PAH/TPPTP–Pt NP treatment cycles of the GCE-Aph/TPPTP–Pt NP electrode. A new film was assembled for each electrochemical measurement.

Electrochemistry. HOR and ORR kinetics was evaluated for the GCE-Aph/TPPTP–Pt NP/(PAH/TPPTP–Pt NP) _{$n-1$} electrodes using a rotating disk electrode (RDE) method.^{11,12} Aqueous 0.1 M perchloric acid was used as the electrolyte, a hydrogen impregnated palladium bead (Pd/H₂) as the reference electrode, and Au foil as the counter electrode. The RDE cell was a 250 mL volume glass cell with a jacket for temperature control. The temperature was maintained at 60 °C with a circulating bath of 1:1 (v/v) mixture of ethylene glycol and water. Electrolyte solutions were saturated with H₂ or O₂ for the HOR and ORR evaluation, respectively, by bubbling gas into the solution through medium porosity glass frits. Electrode rotation rates were controlled using a Pine Instruments AFM-SRX rotator. Electrode potentials were applied using an AU-TOLAB potentiostat. Computer control of the potentiostat and data acquisition was performed with GPES electrochemical software. The current density was calculated using the geometric surface area of the glassy carbon electrode disk (0.196 cm²). The Pd/H electrode was corrected to a reversible hydrogen electrode (RHE) by measuring the potential at which a Pt|Pt cell exhibited zero current under hydrogen in the electrolyte. Platinum loadings were determined for each GCE-Aph/TPPTP–Pt NP/(PAH/TPPTP–Pt NP) _{$n-1$} electrode after electrochemical measurements using Rutherford backscattering spectroscopy (Evans Analytical Group, Sunnyvale, CA) on the glassy carbon electrode directly.

3. Results and Discussion

3.1 Synthesis and Characterization of TPPTP–Pt NPs.

Several protocols were attempted for the synthesis of TPPTP-stabilized Pt NPs including the reduction of K_2PtCl_4 and $\text{H}_2\text{-PtCl}_6 \cdot 6\text{H}_2\text{O}$ with a variety of reductants such as sodium citrate, NaBH_4 , H_2 , CO , and ethylene glycol in the presence of the TPPTP ligand. Reproducible results were obtained by ligand exchange with glycol-stabilized Pt NPs prepared by the method of Wang et al.¹⁵

The TPPTP ligand is known to coordinate to low-valent transition metals exclusively through the phosphine phosphorus,²² and the ligand exchange reaction can be monitored by solution ^{31}P NMR spectroscopy. Coordination of the TPPTP ligand to the platinum nanoparticle is evidenced by the disappearance of the resonance for free phosphine at -6.5 ppm and a new resonance appearing downfield at 3.2 ppm. This is similar to the behavior observed for phosphine ligands coordinated to palladium NPs.²³ However, no $J_{\text{Pt-P}}$ coupling is observed, which is in contrast to the findings of Chaudret et al., who observed complex multiplets in the ^{31}P NMR spectrum and claim a $^1J_{\text{Pt-P}}$ value of 5130 Hz for triphenylphosphine bound to 1.3 nm Pt clusters.²⁴ Schmid et al. have reported the ^{31}P NMR spectrum of the rhodium cluster $\text{Rh}_{55}[\text{P}(t\text{-Bu})_3]_{12}\text{Cl}_{20}$, which shows a singlet at 68 ppm without the expected ^{31}P – ^{103}Rh coupling.²⁵ The narrow line shape and lack of coupling was attributed to fast ligand exchange.

In the case of TPPTP–Pt NPs, no evidence for fast ligand exchange was observed at room temperature by ^{31}P NMR spectroscopy. Addition of free TPPTP (10 mg) to a dispersion of TPPTP–Pt NPs (20 mg) in D_2O (1 mL) caused a shift of the bound TPPTP resonance from 3.2 to 0.5 ppm, but no line broadening for either the free or the bound phosphine resonance is observed. Addition of another 10 mg of TPPTP results in no change in the ^{31}P NMR spectrum. Heating the dispersion to 80 °C resulted in no line broadening of either the free TPPTP or TPPTP–Pt NPs resonance. A second ligand exchange experiment was carried out, involving the addition of 2-mercaptoethanol (0.2 mL, ca. 2500 equiv to TPPTP) to a dispersion of TPPTP–Pt NPs (20 mg) in 0.7 mL of D_2O . After 6 days, no displaced TPPTP was observed by ^{31}P NMR, implying that the TPPTP is tightly bound to the nanoparticle surface. The single-crystal X-ray structure for TPPTP contains 27 waters of hydration in the unit cell,¹³ suggesting that extensive hydrogen bonding may also exist in the ligand shell of the TPPTP–Pt NPs. Extensive hydrogen bonding between the phosphonate groups on the TPPTP–Pt NPs may be prohibiting facile ligand exchange. This may also explain the counterintuitive result that addition of NaOH to an aqueous dispersion of TPPTP–Pt NPs causes them to precipitate from solution, despite the fact that the hexasodium salt of TPPTP is an order of magnitude more soluble in water than is the free acid form of TPPTP. Presumably, the coordination of sodium ions by the phosphonate groups significantly disrupts hydrogen bonding between the phosphonate groups and the solvent molecules. In summary, although reproducible changes in the ^{31}P NMR spectrum accompany the formation of TPPTP-stabilized Pt nanoparticles, the lack of ^{195}Pt – ^{31}P coupling in the phosphine resonance associated with the TPPTP–Pt nanoparticles remains under investigation.

To confirm the platinum–phosphorus interaction of TPPTP-stabilized Pt NPs and the oxidation state of Pt, the TPPTP–Pt NPs were analyzed by X-ray photoelectron spectroscopy. Figure 2a shows the Pt 4f region of the spectrum before electrochemical measurements, which can be deconvoluted into two spin–orbit

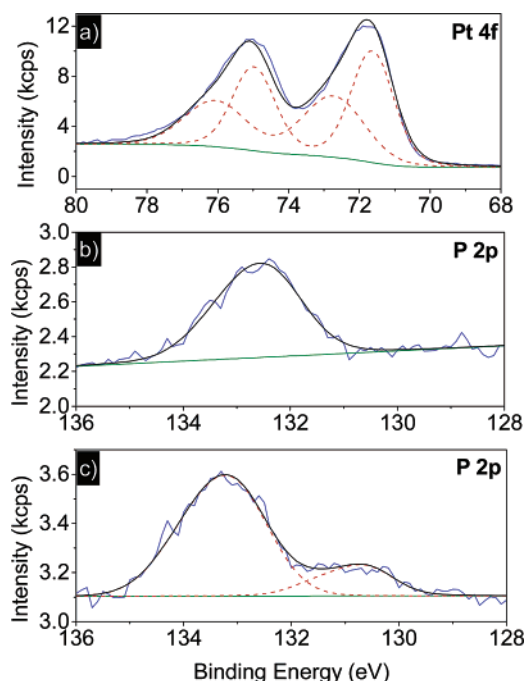


Figure 2. XPS spectra for TPPTP–Pt NPs on grafted carbon paper of (a) Pt 4f, (b) P 2p core levels, and (c) P 2p core level of free TPPTP ligand on grafted carbon paper. Blue line = raw data, black line = total fits, red dashed line = peak components, and green line = background.

doublets. The more intense doublet of Pt $4f_{7/2}$ is measured at a binding energy (BE) of 71.6 eV and, although shifted from bulk platinum metal (Pt $4f_{7/2} = 71.12$ eV),²⁶ is characteristic of Pt in the zero valent state for small platinum nanoparticles.²⁷ The higher BE component of Pt $4f_{7/2}$ at 72.7 eV is assigned to Pt^{II} consistent with PtO or $\text{Pt}(\text{OH})_2$ on the surface of the nanoparticle.²⁸

The P 2p signal of the TPPTP ligand on platinum was also measured (Figure 2b). Only one spin–orbit doublet was observed at 132.4 eV for both the surface-bound phosphine and the surface-bound phosphonate groups of the Pt-bound ligand. This is consistent with a shift of the phosphine P 2p peak to a higher binding energy due to coordination to the platinum metal, resulting from electron donation from the phosphine to the metal. A similar shift has been observed before for 1.3 nm PPh_3 –Pt NPs, where the binding energy of free PPh_3 is observed at 130.9 eV but shifts to 131.8 eV upon coordination to platinum.²⁹ To determine whether a similar binding energy shift occurs for the Pt coordinated TPPTP, a monolayer of free TPPTP ligand electrostatically bound to APh-grafted carbon paper was also analyzed by XPS. Figure 2c shows the P 2p region of the spectrum for free TPPTP, which now shows the expected two spin–orbit doublets at 130.6 eV for the phosphine and 133.0 eV for the three phosphonate groups in a ratio of roughly 1:3, respectively. These results are consistent with the phosphine of the TPPTP ligand coordinated to the surface Pt atoms of the nanoparticle.

Figure 3 shows a high-resolution TEM image of isolated TPPTP–Pt NPs. The histogram resulting from measuring 214 well-separated particles displays a mean particle diameter of 1.7 nm. The electron diffraction pattern (see Supporting Information, Figure S1) exhibited four diffraction rings that correspond to d spacings for the (111), (200), (220), and (311) planes of a face centered–cubic platinum structure.

EXAFS analysis gives additional information about particle size and atomic interactions of the TPPTP–Pt NPs. The EXAFS

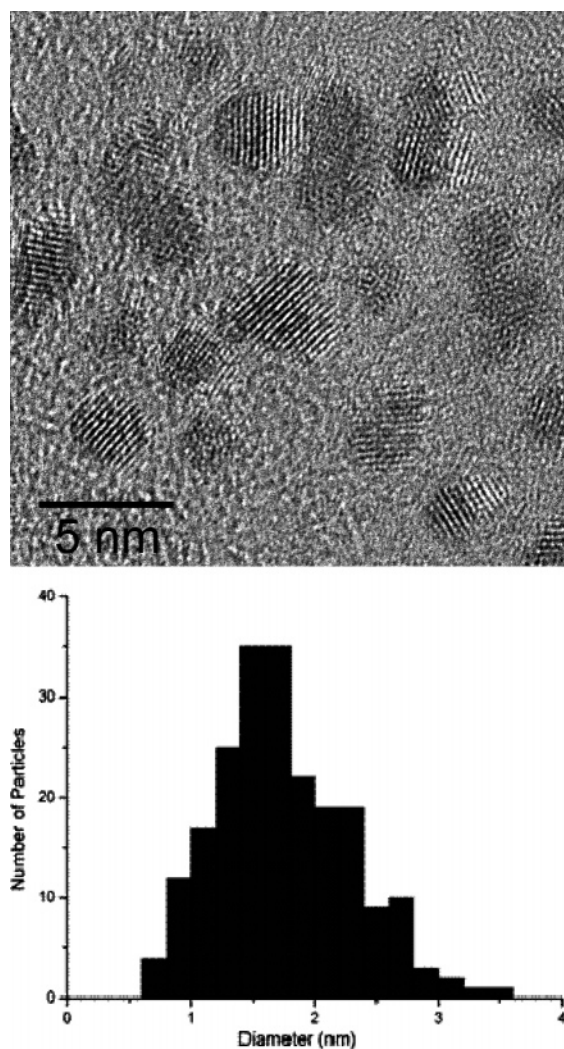


Figure 3. HRTEM of TPPTP-Pt NPs and histogram showing the size distribution of the TPPTP-Pt NPs. The average size is 1.7 ± 0.5 nm.

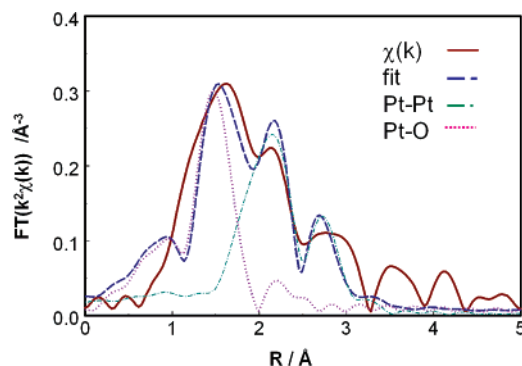


Figure 4. *R*-space fit. Path Pt-Pt: $N = 4.0$, $R = 2.64$ Å, $E_0 = -2.3$ eV, and $\sigma^2 = 0.014$ Å². Path Pt-O: $N = 1.1$, $R = 1.95$ Å, $E_0 = -3.7$ eV, and $\sigma^2 = 0.003$ Å².

data is best fit by the two-shell interactions of Pt-Pt and Pt-O. Figure 4 shows the quality of the fit in the *R*-space using the region $1.4 < R < 3.3$ derived from $\chi(k)$ data in *k*-space from 2 to 11 Å⁻¹ (see Supporting Information, Figure S2). Higher multiple scattering contributions enter above $R = 3$ Å, and an atomic EXAFS contribution³⁰ appears below $R = 1.4$ Å.

The data in Figure 4 are best fit to a 2.65 Å Pt-Pt interaction with a coordination number of 4.0 and a Pt-O interaction with

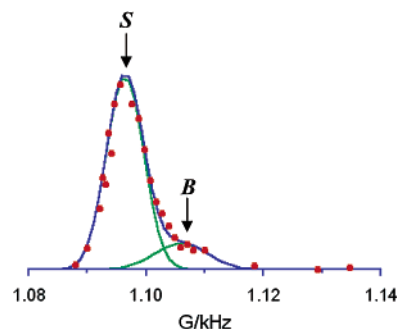


Figure 5. Room temperature ¹⁹⁵Pt solid-state NMR of TPPTP-Pt NPs. Data were acquired on a point-by-point basis (red circles) with the two solid green lines representing deconvoluted peak fitting. The relative ratio of the peaks due to the surface Pt atoms, *S*, to those of the underlying, or bulk, atoms, *B*, suggests that these particles are approximately 1.0 nm in diameter.

a bond distance of 1.95 Å and a coordination number of 1.1 (see Supporting Information). Assuming a spherical particle, this suggests that the NP has a Pt metal core with a diameter of approximately 0.5 nm containing around ~five to seven atoms, with an oxidized surface that is reduced to metal upon exposure to H₂ and the electrolyte.

The small Pt-Pt coordination number is indirect evidence for the presence of TPPTP ligands bound to Pt metal on the surface of the nanoparticles. The Pt-P contribution could not be modeled directly in the fit with the Pt-Pt and Pt-O because each interaction requires four parameters, but only 10 parameters are allowed with the Nyquist theorem. The Pt-P contribution at 2.5 Å is also difficult to separate from the Pt-Pt contribution at 2.65 Å because of the weaker scattering signal. The Pt-P coordination number should be on the order of 0.14 based on the elemental analysis results showing approximately seven platinum atoms per TPPTP ligand. Evidence for a Pt-P interaction comes from the somewhat large Debye-Waller factor σ^2 , a measure of structural disorder, which is consistent with strong interaction of the surface atoms with adsorbed molecules, as is the short Pt-Pt bond length (2.65 Å vs 2.78 Å in bulk Pt metal), which tends to decrease with decreasing particle size and interaction with surface-bound molecules.³¹ Others have shown that for Ru nanoparticles, 4 nm particles capped with thiols had a lower coordination number than 2 nm particles coated with polyol, due to the disorder introduced by the strong thiol ligands.³² Therefore, the Pt particles are likely larger than 0.5 nm, making the EXAFS data consistent with the findings of NMR and TEM.

The degree to which stabilizing ligands or other adsorbate molecules interact with the surface atoms of a platinum particle can be observed by solid-state ¹⁹⁵Pt NMR.³³ Unlike most nonmetals, the NMR of a transition metal, such as platinum, reveals a resonance peak whose position is not solely due to chemical shifts but also has a contribution from the Knight shift. The Knight shift is due to polarization of the spins of the conduction electrons in the metal and has the greatest influence on the position of the resulting metal NMR line in most bulk metals.³⁴

Figure 5 depicts the room-temperature solid-state ¹⁹⁵Pt NMR of the TPPTP-stabilized Pt NPs acquired on a point-by-point basis and the fit to the data (solid lines) according to the healing layer model³⁵ with K_0 , the surface layer Knight shift, m , the number of layers defining the healing length, and the Gaussian widths as the fitting parameters (see Supporting Information). The nonsymmetrical ¹⁹⁵Pt NMR line shape was deconvoluted to separate peaks, each with different shifts; those due to the

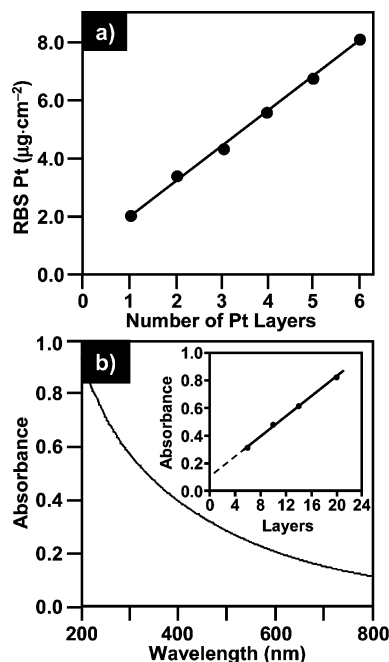


Figure 6. (a) Platinum loading ($\mu\text{g}/\text{cm}^2$) as measured by Rutherford backscattering spectroscopy vs number of (TPPTP–Pt NPs)_n ($n = 1$ –6) layers for each electrode. Slope = $1.217 \mu\text{g cm}^{-2}$, intercept = $0.6733 \mu\text{g cm}^{-2}$, and $R^2 = 0.9974$. (b) UV–vis spectrum of an EDA/TPPTP–Pt NP/(PAH/TPPTP–Pt NP)₁₉ multilayer film on fused silica. Inset: linear plot of absorbance at 223 nm vs number of TPPTP–Pt NP layers. Slope = 0.0361 , intercept = 0.105 , and $R^2 = 0.9992$.

surface atoms, *S*, and those due to the underlying subsurface bulk atoms, *B*. From integrated areas of these peaks, it is possible to calculate the relative percentage of surface atoms in the nanoparticle cluster. From these data, a particle size of approximately 1.0 nm in diameter was calculated.

This result indicates that only the inner core of atoms resemble bulk metal, while the majority of the platinum atoms are nonmetallic in nature due to strong electronic coupling with surface-bound molecules. This is similar to the effect of CO adsorption to the surfaces of transition metal clusters, which has been attributed to alterations in the Fermi level local density of states (E_F -LDOS) of the metal upon binding to the ligand.³⁶ Such distortions of the electronic structure by the adsorbed ligands have important implications for their electrocatalytic activity.

3.2 Electrochemistry. Electrode Assembly. To determine their electrocatalytic activity, multilayers of TPPTP–Pt NPs were assembled via electrostatic layer-by-layer deposition with PAH on a protonated APh-modified glassy carbon electrode (vide supra). Surface $\text{p}K_a$ measurements³⁷ made for TPPTP–Pt NPs bound to model ITO surfaces gave estimated values of $\text{p}K_{a1} 2.0 \pm 0.2$ and $\text{p}K_{a2} 8.4 \pm 0.3$ for the P–O groups of the coordinated TPPTP. Analogous experiments using PAH-coated ITO gave similar $\text{p}K_a$ s of 1.8 ± 0.2 and 9.0 ± 0.3 , respectively. This suggests an average charge of approximately -1.5 units/TPPTP group under the acidic conditions (i.e., $0.01 \text{ M HCl}/0.01 \text{ M NaCl}_{(\text{aq})}$) used during the electrode film assembly, consistent with an electrostatic film fabrication mechanism. Voltammetry at 2, 4, and 6 layer films of TPPTP–Pt NPs under Ar (see Supporting Information, Figure S4) shows an increase in the current density for H desorption as a function of the number of TPPTP–Pt NP layers, indicating an increase in total platinum on the electrode surface. The plot of Pt loading versus number of TPPTP–Pt NPs layers (Figure 6a) shows that the platinum loading increases linearly with each layer deposited.

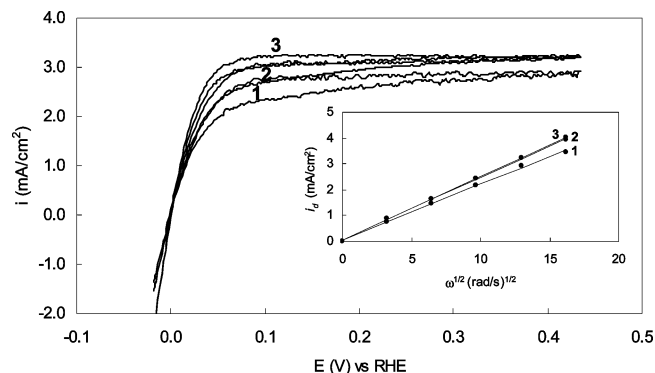


Figure 7. RDE voltammetry of the HOR at 1, 2, and 3 layer films of TPPTP–Pt NPs in H_2 -saturated 0.1 M HClO_4 at 60°C , 1600 rpm, obtained at a sweep rate of 20 mV s^{-1} . Inset: plot of i_d vs $\omega^{1/2}$ for the HOR at 0.4 V .

However, the plot does not intersect at the origin, due to a relatively higher number density of TPPTP–Pt NPs deposited in the first layer relative to each additional layer, resulting in the positive offset of the line.

To further confirm that polymer–nanoparticle bilayers on the GCE were being uniformly deposited, the solutions used for deposition on the electrodes were used to deposit bilayers on fused silica (FS) slides primed with an EDA siloxane self-assembled monolayer film. The absorbance of 1–20 TPPTP–Pt NP/PAH bilayers was monitored by UV–vis spectrometry at 223 nm (20 bilayers shown, Figure 6b). The linearity of the plot of absorbance versus number of bilayers (inset in Figure 6b) agrees well with the RBS data and confirms uniform film growth and deposition of the PAH and TPPTP–Pt NP layers. The absence of plasmon resonance bands in the UV–vis spectrum indicates that there is no aggregation³⁸ of the TPPTP–Pt NPs in the film and is consistent with the presence of sub-3 nm particles in accordance with solid-state NMR, TEM, and EXAFS analyses.

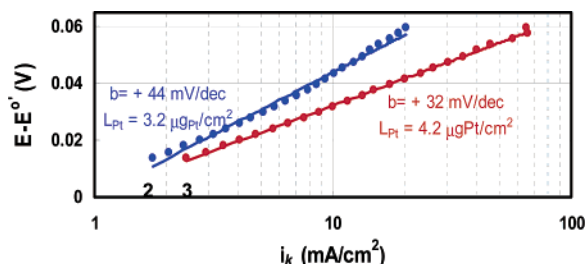
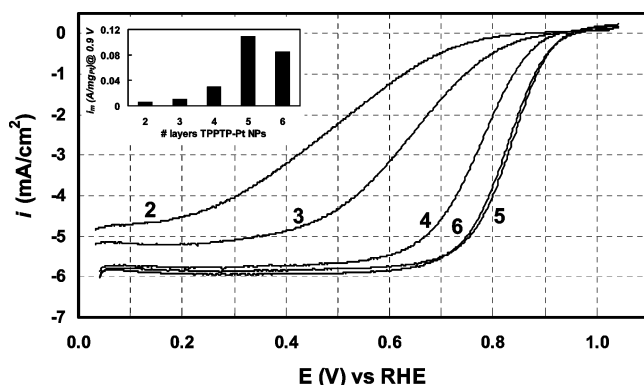
H_2 Oxidation. Voltammetry of the HOR at 1, 2, and 3 layer films of TPPTP–Pt NPs is shown in Figure 7. The catalysts exhibit high activity, indicating that the catalytic sites for hydrogen adsorption are not blocked by the ligands, and charge and mass transport through these films is not hindered. Further inspection of Figure 7 shows that the anodic current rises sharply and reaches a plateau at relatively low overpotentials similar to Pt(110), the most active crystal face of Pt for the HOR.³⁹ At higher overpotentials, the current is determined by the diffusion of H_2 through the acidic media, and the theoretical value of the diffusion-limited current at the RDE, i_d , is given by the Levich equation (eq 3)⁴⁰

$$i_d = 0.62nFD^{2/3}\nu^{-1/6}c_0\omega^{1/2} \quad (3)$$

where n is the number of electrons exchanged in the reaction, D is the diffusion coefficient of H_2 in 0.1 M HClO_4 at 60°C , ν is the kinematic viscosity of the electrolyte, c_0 is the bulk concentration of H_2 in solution, and ω is the angular velocity of the RDE. A minimum of 2 layers of TPPTP–Pt NPs, which corresponds to a platinum loading of $3.2 \mu\text{g}/\text{cm}^2$, is required to reach the theoretical diffusion-limited current density of $3.1 \text{ mA}/\text{cm}^2$ at 1600 rpm as determined from the Levich equation. The limiting currents at 2 and 3 layer films of TPPTP–Pt NPs obey the Levich equation and increase linearly with the square root of rotation rate from 100 to 2500 rpm (inset, Figure 7). At only 1 layer of TPPTP–Pt NPs, the HOR current still increases linearly with $\omega^{1/2}$ but plateaus at values slightly below those

TABLE 1: Kinetic Parameters for the ORR on (TPPTP-Pt NPs/PAH) Electrodes in 0.1 M HClO₄ at 60 °C^a

layers of TPPTP-Pt NPs	Tafel slope 0.92–0.85 V (mV/dec)	Tafel slope 0.83–0.73 V (mV/dec)	kinetic current, $i_k(0.9V)$ (mA/cm ²)	mass-specific activity, $i_m(0.9V)$ (A/mg _{Pt})	Pt loading (μg _{Pt} /cm ²)
4	−75	−109	−0.17	0.03	5.6
5	−67	−104	−0.72	0.11	6.6
6	−71	−101	−0.65	0.08	8.1
Pt(111) ⁴³	−59	−118	—	—	—
20% Pt/VC ¹¹	—	—	−3.0	0.19	14.3

^a Sweep rate = 20 mV/s.**Figure 8.** Tafel plot for the HOR at 2 and 3 layer films of TPPTP-Pt NPs in H₂-saturated 0.1 M HClO₄ at 60 °C.**Figure 9.** RDE voltammetry of the ORR at 2–6 layer films of TPPTP-Pt NPs in O₂-saturated 0.1 M HClO₄ at 60 °C, 1600 rpm, obtained at a sweep rate of 20 mV s^{−1}. Inset: mass-specific activities at 0.9 V vs layers of TPPTP-Pt NPs (2–6 layers).

predicted for a purely diffusion-controlled reaction, indicating that not enough active platinum was accessible at the electrode surface to oxidize all the available hydrogen.

The standard current–overpotential relation for a reaction under mixed diffusion–kinetic control is described by eq 4⁴⁰

$$i/i_o = (1 - i/i_{l,a})e^{-\alpha n F \eta / RT} - (1 - i/i_{l,c})e^{(1-\alpha)n F \eta / RT} \quad (4)$$

where i is current, i_o is the exchange current, $i_{l,a}$ and $i_{l,c}$ are the limiting anodic and cathodic currents, respectively, n is the number of electrons involved in the slow electron-transfer step, α is the transfer coefficient for the reaction (typically 1/2), and η is the overpotential, alternately expressed as $E - E^\circ$, where E is the potential and E° is the formal potential for the reaction. At sufficiently large η , the cathodic term becomes negligible for the HOR, and eq 4 can be rearranged to yield the familiar Tafel form (eq 5)⁴⁰

$$\eta = (2.303RT/\alpha n F) \log i_o - (2.303RT/\alpha n F) \log i_k \quad (5)$$

where i_k is the kinetic current that can be related to the Tafel current by eq 6 for a reaction under mixed kinetic–diffusion control. If the rate-determining step is a slow electron transfer, plotting η versus the log term yields a straight line with a Tafel

slope of $59/\alpha n$ mV at 298 K or $66/\alpha n$ mV at 333 K.

$$i_k = ii_{l,a}/(i_{l,a} - i) \quad (6)$$

We calculate Tafel slopes of +44 and +32 mV/dec for 2 and 3 layer TPPTP-Pt NP electrodes, respectively (Figure 8). At low overpotentials, Marković and Ross report Tafel slopes for the HOR on various Pt crystal faces: +28 mV/dec for Pt-(110), +37 mV/dec for Pt(100), and +74 mV/dec for Pt(111).³⁹ They also concluded that the different crystal faces utilize different reaction mechanisms for the HOR. While the TPPTP-Pt NPs display several crystal faces, the Tafel slope for the 3 layer film of TPPTP-Pt NPs indicates a similar HOR mechanism as to Pt(110). We interpret the higher Tafel slope for the 2 layer film of TPPTP-Pt NPs not to a change in reaction mechanism, but rather to a Pt-limited reaction condition.

O₂ Reduction. Figure 9 compares the anodic sweeps of the ORR voltammetry on 2–6 layer films of TPPTP-Pt NPs at 60 °C. At larger overpotentials (potentials more negative than ~0.7 V for 4–6 layers of TPPTP-Pt NPs), the current is determined by the diffusion of O₂ through the acidic media, and the theoretical value of i_d for an RDE is given by the Levich equation (eq 3). A minimum of 4 layers of TPPTP-Pt NPs, which corresponds to a platinum loading of 5.6 μg_{Pt}/cm², is required to reach the theoretical diffusion-limited current density of −6.0 mA/cm² at 1600 rpm, as determined from the Levich equation using the diffusion coefficient of oxygen ($D = 1.93 \times 10^{-5}$ cm²/s), kinematic viscosity of the electrolyte ($\nu = 1.009 \times 10^{-2}$ cm²/s), and the concentration of dissolved oxygen in solution ($c_0 = 1.26 \times 10^{-6}$ mol/cm³).⁴¹ Five layers of TPPTP-Pt NPs yield the highest mass-specific activity, i_m , at 0.9 V of 0.11 A/mg_{Pt} (inset, Figure 9) as calculated from the kinetic current, i_k (eq 6), and normalized with the platinum loading of 6.6 μg_{Pt}/cm².

As the amount of TPPTP-Pt NPs layers is increased to 6, the mass-specific activity drops to 0.09 A/mg_{Pt} at 0.9 V (inset, Figure 9). Although more platinum is on the electrode surface in 6 layers of TPPTP-Pt NPs, it appears that a maximum current density is reached with 5 layers. No electronic resistivity is evident in voltammetry performed in argon (see Supporting Information). Although the films are quite thin ranging from 6 to 19 nm for 1 and 6 layer TPPTP-Pt NPs electrodes, respectively, it is possible that gas diffusion into the three-dimensional architecture is inefficient. However, more probable is the presence of chloride ions during the preparation of these films that have been shown to impede ORR activity.⁴²

The slope of a linear plot derived from the Levich equation can be used to determine the number of electrons involved in the ORR (see Supporting Information, Figure S5). The experimental values of 0.44, 0.45, and 0.45 (mA/cm²)rds^{−1/2} for 4–6 layers of TPPTP-Pt NPs agree well with the complete reduction of O₂ by four electrons. Two and 3 layers of TPPTP-Pt NPs had much lower slopes of 31 and 34 (mA/cm²)rds^{−1/2},

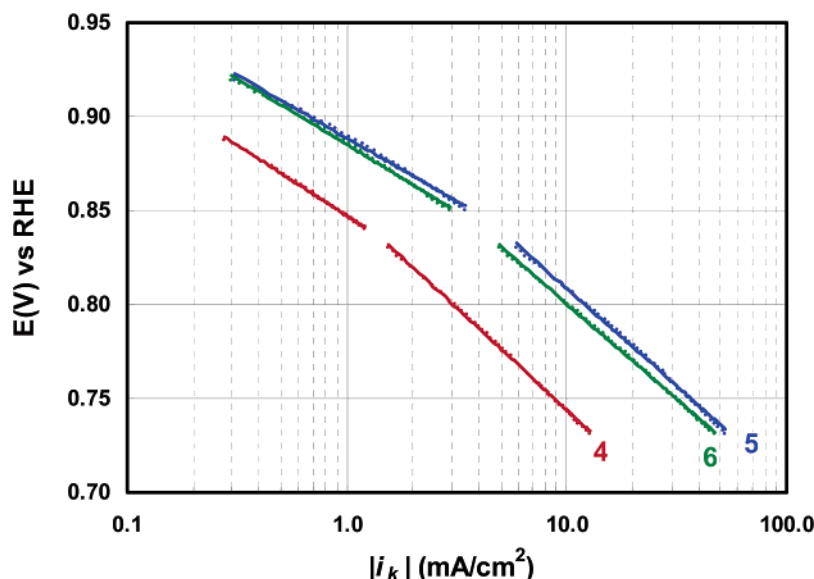


Figure 10. Tafel plots for data in Figure 9 (only 4–6 layers of TPPTP–Pt NPs).

respectively, indicating that not enough active platinum was accessible at the electrode surface to reduce all available O_2 to water.

Figure 10 shows a logarithmic plot of the mass-transport corrected currents in the Tafel region for ORR at 4–6 layer TPPTP–Pt NPs electrodes. It is clear from the plot that there are two distinct slopes at higher ($E > 0.85$ V) and lower potentials ($E < 0.83$ V), indicating that the rate-limiting step changes. The intrinsic Tafel slope for Pt with no adsorbates other than the ORR intermediates is -118 mV/dec.⁴³ Deviations in the Tafel slope at higher potentials in perchloric acid are attributed to OH adsorption, which hinders oxygen reduction.^{43,44} The experimental values of -75 , -67 , and -71 mV/dec at higher potentials for 4–6 layers TPPTP–Pt NPs, respectively, are consistent with results seen for ORR on Pt(111) (Table 1). Correlations of Tafel slopes and voltammetry between well-defined single-crystal electrodes, such as Pt(111), and Pt NPs suggest that ORR mechanisms are the same for each electrode.⁴³

Finally, to confirm the stability of the multilayer electrodes during these experiments, a 5 layer TPPTP–Pt NPs electrode was cycled between 1.0 and 0 V at 20 mV/s for 20 cycles in 0.1 M $HClO_4$ at 60 °C, and no appreciable loss in the catalytic current of oxygen reduction was observed. Additionally, no change in the mass-specific activity at 0.9 V was observed after exposure to air for several days. Furthermore, XPS spectra were collected on carbon paper modified with a monolayer of TPPTP–Pt NPs before and after electrochemical measurements to confirm that the TPPTP ligand remains intact. No measurable change was observed in the Pt 4f or P 2p region after electrochemical measurements, indicating that the ligands remain unchanged.

4. Conclusion

In summary, a reproducible synthesis of platinum NPs stabilized with a water-soluble phosphine has been developed by ligand exchange with preformed glycol-stabilized platinum nanoparticles. XPS and elemental analyses confirm the presence of TPPTP on the Pt nanoparticle surface with a Pt/P ratio of $\sim 7:1$. The Pt NPs are nominally 1.7 nm crystallites with an fcc structure. Both EXAFS and solid-state ^{195}Pt NMR analyses show a high percentage of surface to bulk atoms, which is most

consistent with a flattened or truncated cubooctahedral geometry, with significant electronic interaction of the surface atoms with adsorbed molecular species. The adsorbed TPPTP ligands confer sufficient stability and water solubility on the Pt nanoparticles to permit their use in the fabrication of structured multilayered films with PAH via electrostatic LBL techniques on both fused silica and glassy carbon electrode surfaces, as shown by UV–vis and RBS spectroscopic analysis, respectively.

Multilayer films comprising alternating TPPTP–Pt NPs/PAH layers were shown to be active electrocatalysts for both hydrogen oxidation and oxygen reduction. Only 3 layers of TPPTP–Pt NPs, corresponding to $4.2 \mu g_{Pt}/cm^2$, is required to reach diffusion-limited kinetics for the HOR. Importantly, the phosphine ligands shown to be bound to the surface of the platinum nanoparticle do not appear to hinder their electrocatalytic activity, and in fact, improvements may be possible with rational choice and design of new ligands. Density functional theory (DFT) calculations suggest that basic supports promote hydrogen binding to Pt, while acidic supports promote oxygen binding.⁴⁵ The latter effect is especially important in improving ORR kinetics since ORR activity has been shown to correlate well with the oxygen chemisorption energy.⁴⁶ This suggests that it is possible to tune the reactivity of Pt nanoparticles by varying the π -acidity and σ -basicity of the organic ligands bound to the surface of the nanoparticle.

The more difficult ORR requires a minimum of 4 layers TPPTP–Pt NPs with a total platinum loading of $5.6 \mu g_{Pt}/cm^2$ to completely reduce oxygen by four electrons. A maximum current density for oxygen reduction was reached after 5 layers resulting in a mass-specific activity, i_m , of $0.11 A/mg_{Pt}$ at 0.9 V. Although the mass-specific activities for the ORR were close to that of state-of-the-art Pt–VC PEMFCs, the kinetic current densities are presently about an order of magnitude lower (Table 1). The removal of chloride ions and replacement of PAH with an electronically conducting polymer (e.g., polyaniline) should improve charge transfer between TPPTP–Pt NPs and glassy carbon electrode while maintaining good mass transfer to catalyst sites. Our TPPTP–Pt NPs catalyst architectures compare well to state-of-the-art PEMFC Pt–VC catalysts, but our results cannot be directly compared to similar multilayer or ligand-stabilized catalyst electrodes as the other reports lack comparable kinetic data or do not specify the total platinum loading.

The use of well-characterized water-soluble NPs formed *ex situ* has the advantage of facilitating the incorporation of the NPs in different architectures, and we are presently investigating the use of high-surface area, mesoporous electrodes materials, such as those formed using conductive metal or carbon foams.⁴⁷ We are continuing our investigations of ligand-stabilized nanoparticles to more fully exploit and realize their full potential as electrocatalysts.

Acknowledgment. We thank the Office of Naval Research for support under the Naval Research Laboratory Core (Nanoscience) Program. The authors are grateful to Drs. Margaret Teliska for collecting EXAFS data, Scott Trammell for surface pK_a measurements, and Dmitri Petrovykh for help with XPS analyses. C.N.K. thanks the National Academy of Sciences for a National Research Council postdoctoral fellowship.

Supporting Information Available: TEM electron diffraction pattern, EXAFS k -space fits, a more detailed discussion of the solid-state ^{195}Pt NMR fit for the TPPTP–Pt NPs, voltammetry in argon for 2, 4, and 6 layer TPPTP–Pt NP electrodes, and the ORR Levich plot at 2–6 layer TPPTP–Pt NP electrodes. This material is available free of charge via the Internet at <http://pubs.acs.org>.

References and Notes

- (1) Ferreira, P. J.; la O', G. J.; Shao-Horn, Y.; Morgan, D.; Makharia, R.; Kocha, S.; Gasteiger, H. A. *J. Electrochem. Soc.* **2005**, *152*, 2256–2271.
- (2) Bernardi, D. M.; Verbrugge, M. W. *J. Electrochem. Soc.* **1992**, *139*, 2477–2491.
- (3) Gasteiger, H. A.; Panels, J. E.; Yan, S. G. *J. Power Sources* **2004**, *127*, 162–171.
- (4) (a) Zhang, J.; Vukmirovic, M. B.; Sasaki, K.; Nilekar, A. U.; Mavrikakis, M.; Adzic, R. R. *J. Am. Chem. Soc.* **2005**, *127*, 12480–12481. (b) Zhang, J.; Vukmirovic, M. B.; Xu, Y.; Mavrikakis, M.; Adzic, R. R. *Angew. Chem., Int. Ed.* **2005**, *44*, 2132–2135. (c) Zhang, J.; Lima, F. H. B.; Shao, M. H.; Sasaki, K.; Wang, J. X.; Hanson, J.; Adzic, R. R. *J. Phys. Chem. B* **2005**, *109*, 22701–22704. (d) Marković, N. M.; Schmidt, T. J.; Stamenković, V.; Ross, P. N. *Fuel Cells* **2001**, *1*, 105–116. (e) Meng, H.; Shen, P. K. *J. Phys. Chem. B* **2005**, *109*, 22705–22709. (f) Anderson, A. B.; Roques J.; Mukerjee, S.; Murthi, V. S.; Marković, N. M.; Stamenković, V. *J. Phys. Chem. B* **2005**, *109*, 1198–1203. (g) Stamenković, V.; Schmidt, T. J.; Ross, P. N.; Marković, N. M. *J. Phys. Chem. B* **2002**, *106*, 11970–11979. (h) Gulla, A. F.; Saha, M. S.; Allen, R. J.; Mukerjee, S. *J. Electrochem. Soc.* **2006**, *153*, 366–371. (i) Koffi, R. C.; Coutanceau, C.; Garnier, E.; Leger, J.-M.; Lamy, C. *Electrochim. Acta* **2005**, *50*, 4117–4127. (j) Sode, A.; Li, W.; Yang, Y.; Wong, P. C.; Gyenge, E.; Mitchell, K. A. R.; Bizzotto, D. J. *Phys. Chem. B* **2006**, *110*, 8715–8722. (k) Ralph, T. R.; Hogarth, M. P. *Platinum Metals Rev.* **2002**, *26*, 3–14.
- (5) (a) Fernandez, J. L.; Raghuveer, V.; Manthiram, A.; Bard, A. J. *J. Am. Chem. Soc.* **2005**, *127*, 13100–13101. (b) Raghuveer, V.; Manthiram, A.; Bard, A. J. *J. Phys. Chem. B* **2005**, *109*, 22909–22912. (c) Fernandez, J. L.; Walsh, D. A.; Bard, A. J. *J. Am. Chem. Soc.* **2005**, *127*, 357–365. (d) Wang, B. *J. Power Sources* **2005**, *152*, 1–15.
- (6) Giordano, N.; Passalacqua, E.; Pino, L.; Arico, A. S.; Antonucci, V.; Vivaldi, M.; Kinoshita, K. *Electrochim. Acta* **1991**, *36*, 1979–1984.
- (7) Schmid, G.; Maihack, V.; Lantermann, F.; Peschel, S. *J. Chem. Soc., Dalton Trans.* **1996**, 589–595.
- (8) (a) Modrow, H.; Bucher, S.; Hormes, J.; Brinkmann, R.; Bönemann, H. *J. Phys. Chem. B* **2003**, *107*, 3684–3689. (b) Bucher, S.; Hormes, J.; Modrow, H.; Brinkmann, R.; Waldöfner, N.; Bönemann, H.; Beuermann, L.; Krischok, S.; Maus-Friedrichs, W.; Kemper, V. *Surf. Sci.* **2002**, *497*, 321–332. (c) Larsson, J. A.; Nolan, M.; Greer, J. C. *J. Phys. Chem. B* **2002**, *106*, 5931–5937. (d) Kataby, G.; Koltypin, Y.; Rothe, J.; Hormes, J.; Felner, I.; Cao, X.; Gedanken, A. *Thin Solid Films* **1998**, *333*, 41–49.
- (9) (a) Ye, H.; Crooks, R. M. *J. Am. Chem. Soc.* **2005**, *127*, 4930–4934. (b) Zhao, M.; Crooks, R. M. *Adv. Mater.* **1999**, *11*, 217–220.
- (10) Some recent examples of polyelectrolyte multilayer structures for fuel cell applications: (a) Farhat, T. R.; Hammond, P. T. *Chem. Mater.* **2006**, *18*, 41–49. (b) Karam, P.; Estephen, Z. G.; El Haraketh, M.; Houry, M.; Halaoui, L. I. *Electrochem. Solid-State Lett.* **2006**, *9*, 144–146. (c) Markarian, M. Z.; El Haraketh, M.; Halaoui, L. I. *J. Phys. Chem. B* **2005**, *109*, 11616–11621. (d) Pan, M.; Tang, H. L.; Jiang, S. P.; Liu, Z. *Electrochem. Commun.* **2005**, *7*, 119–124. (e) Huang, M.; Shao, Y.; Sun, X.; Chen, H.; Liu, B.; Dong, S. *Langmuir* **2005**, *21*, 323–329. (f) Shen, Y.; Liu, J.; Wu, A.; Jiang, J.; Bi, L.; Liu, B.; Li, Z.; Dong, S. *Langmuir* **2003**, *19*, 5397–5401. (g) Choi, J.-H.; Park, K.-W.; Lee, H.-K.; Kim, Y.-M.; Lee, J.-S.; Sung, Y.-E. *Electrochim. Acta* **2003**, *48*, 2781–2789. (h) Shen, Y.; Liu, J.; Wu, A.; Jiang, J.; Bi, L.; Liu, B.; Li, Z.; Dong, S. *Chem. Lett.* **2002**, 550–551.
- (11) Gasteiger, H. A.; Kocha, S. S.; Sompalli, B.; Wagner, F. T. *Appl. Catal., B* **2005**, *56*, 9–35.
- (12) Paulus, U. A.; Schmidt, T. J.; Gasteiger, H. A.; Behm, R. J. *J. Electroanal. Chem.* **2001**, *495*, 134–145.
- (13) (a) Dressick, W. J.; George, C.; Brandow, S. L.; Schull, T. L.; Knight, D. A. *J. Org. Chem.* **2000**, *65*, 5059–5062. (b) Schull, T. L.; Brandow, S. L.; Dressick, W. J. *Tetrahedron Lett.* **2001**, *42*, 5373–5376.
- (14) Broxton, T. J.; Bunnett, J. F.; Paik, C. H. *J. Org. Chem.* **1977**, *42*, 643–649.
- (15) Wang, Y.; Ren, J.; Deng, K.; Gui, L.; Tang, Y. *Chem. Mater.* **2000**, *12*, 1622–1627.
- (16) Woehrle, G. H.; Brown, L. O.; Hutchison, J. E. *J. Am. Chem. Soc.* **2005**, *127*, 2172–2183.
- (17) Hesse, R.; Chesse, T.; Szargan, R. *Fresenius' J. Anal. Chem.* **1999**, *365*, 48–54.
- (18) IFEFFIT software from: Ravel, B.; Newville, N. *J. Synchrotron Radiat.* **2005**, *12*, 537–541.
- (19) Chen, M.-S.; Dulcey, C. S.; Chrisey, L. A.; Dressick, W. J. *Adv. Funct. Mater.* **2006**, *16*, 774–783.
- (20) Chen, M.-S.; Brandow, S. L.; Dulcey, C. S.; Dressick, W. J.; Taylor, G. N.; Bohland, J. F.; Georger, J. H., Jr.; Pavelchek, E. K.; Calvert, J. M. *J. Electrochem. Soc.* **1999**, *146*, 1421–1430.
- (21) (a) Delamar, M.; Hitmi, R.; Pinson, J.; Savéant, J. M. *J. Am. Chem. Soc.* **1992**, *114*, 5883–5884. (b) Allongue, P.; Delamar, M.; Desbat, B.; Fagebaume, O.; Hitmi, R.; Pinson, J.; Savéant, J. M. *J. Am. Chem. Soc.* **1997**, *119*, 201–207.
- (22) (a) Schull, T. L.; Butcher, R.; Dressick, W. J.; Brandow, S. L.; Byington, L. K.; Knight, D. A. *Polyhedron* **2004**, *23*, 1375–1378. (b) Harper, B. A.; Knight, D. A.; George, C.; Brandow, S. L.; Dressick, W. J.; Dulcey, C. S.; Schull, T. L. *Inorg. Chem.* **2003**, *42*, 516–524. (c) Schull, T. L.; Fetting, J. C.; Knight, D. A. *Inorg. Chem.* **1996**, *35*, 6717–6723.
- (23) Son, S. U.; Jang, Y.; Yoon, K. Y.; Kang, E.; Hyeon, T. *Nano Lett.* **2004**, *4*, 1147–1151.
- (24) Amiens, C.; de Caro, D.; Chaudret, B.; Bradley, J. S.; Mazel, R.; Roucau, C. *J. Am. Chem. Soc.* **1993**, *116*, 11638–11639.
- (25) Schmid, G.; Giebel, U.; Huster, W. *Inorg. Chim. Acta* **1984**, *84*, 97–102.
- (26) Powell, C. J. *Appl. Surf. Sci.* **1995**, *89*, 141–149.
- (27) (a) Mason, M. G.; Gerenser, L. J.; Lee, S. T. *Phys. Rev. Lett.* **1977**, *39*, 288–291. (b) Cheung, T. T. P. *Surf. Sci.* **1984**, *140*, 151–164.
- (28) Kim, K. S.; Winograd, N.; Davis, R. E. *J. Am. Chem. Soc.* **1971**, *93*, 6296–6297.
- (29) Fu, X.; Wang, Y.; Wu, N.; Gui, L.; Tang, Y. *J. Colloid Interface Sci.* **2001**, *243*, 326–330.
- (30) Ramaker, D. E.; de Graaf, J.; van Veen, J. A. R.; Koningsberger, D. C. *J. Catal.* **2001**, *203*, 7–17.
- (31) Ankudinov, A. L.; Rehr, J. J.; Low, J. J.; Bare, S. R. *J. Chem. Phys.* **2002**, *116*, 1911–1919.
- (32) Chakroune, N.; Viau, G.; Ammar, S.; Poul, L.; Veautier, D.; Chehimi, M. M.; Mangeney, C.; Villain, F.; Fiévet, F. *Langmuir* **2005**, *21*, 6788–6796.
- (33) (a) Slichter, C. P. *Philos. Mag. B* **1999**, *79*, 1253–1261. (b) Stokes, H. T.; Makowka, C. D.; Wang, P.-K.; Rudaz, S. L.; Slichter, C. P. *J. Mol. Catal.* **1983**, *20*, 321–325.
- (34) Pronk, B. J.; Brom, H. B.; Ceriotti, A.; Longoni, G. *Solid State Commun.* **1987**, *64*, 7–10.
- (35) van der Klink, J. J.; Brom, H. B. *Prog. NMR Spectrosc.* **2000**, *36*, 89–201.
- (36) Tong, Y. Y.; Rice, C.; Godbout, N.; Wieckowski, A.; Oldfield, E. *J. Am. Chem. Soc.* **1999**, *121*, 2996–3003.
- (37) Liu, J.; Cheng, L.; Liu, B.; Dong, S. *Langmuir* **2000**, *16*, 7471–7476.
- (38) Schmitt, J.; Decher, G.; Dressick, W. J.; Brandow, S. L.; Geer, R. E.; Shashidhar, R.; Calvert, J. M. *Adv. Mater.* **1997**, *9*, 61–65.
- (39) Marković, N. M.; Grgur, B. N.; Ross, P. N. *J. Phys. Chem. B* **1997**, *101*, 5405–5413.
- (40) Bard, A. J.; Faulkner, L. R. *Electrochemical methods: fundamentals and applications*; Wiley-Interscience: New York, 1980.
- (41) Marković, N. M.; Gasteiger, H. A.; Grgur, B. N.; Ross, P. N. *J. Electroanal. Chem.* **1999**, *467*, 157–163.
- (42) Schmidt, T. J.; Paulus, U. A.; Gasteiger, H. A.; Behm, R. J. *J. Electroanal. Chem.* **2001**, *508*, 41–47.
- (43) Wang, J. X.; Marković, N. M.; Adzic, R. R. *J. Phys. Chem. B* **2004**, *108*, 4127–4133.
- (44) Mayrhofer, K. J. J.; Blizanac, B. B.; Arenz, M.; Stamenković, V. R.; Ross, P. N.; Marković, N. M. *J. Phys. Chem. B* **2005**, *109*, 14433–14440.

(45) Oudenhuijzen, M. K.; van Bokhoven, J. A.; Ramaker, D. E.; Koningsberger, D. C. *J. Phys. Chem. B* **2004**, *108*, 20247–20254.

(46) Stamenković, V.; Mun, B. S.; Mayrhofer, K. J. J.; Ross, P. N.; Marković, N. M.; Rossmeisl, J.; Greeley, J.; Nørskov, J. K. *Angew. Chem., Int. Ed.* **2006**, *45*, 2897–2901.

(47) (a) Tuchinskiy, L. *J. Adv. Mater.* **2005**, *37*, 60–65. (b) Zhao, P.; Zhang, H. M.; Zhou, H. T.; Yi, B. L. *Electrochim. Acta* **2005**, *51*, 1091–1098. (c) Lee, D.; Lee, J.; Kim, J.; Kim, J.; Na, H. B.; Kim, B.; Shin, C.-H.; Kwak, J. H.; Dohnalkova, A.; Grate, J. W.; Hyeon, T.; Kim, H.-S. *Adv. Mater.* **2005**, *17*, 2828–2833.